ARTICLE OPEN

Impact of the Pacific sector sea ice loss on the sudden stratospheric warming characteristics

Jiarong Zhang [1 ✉], Yvan J. Orsolini[2,3], Varavut Limpasuvan[1] and Jinro Ukita[4]

The atmospheric response to Arctic sea ice loss remains a subject of much debate. Most studies have focused on the sea ice retreat in the Barents-Kara Seas and its troposphere-stratosphere influence. Here, we investigate the impact of large sea ice loss over the Chukchi-Bering Seas on the sudden stratospheric warming (SSW) phenomenon during the easterly phase of the Quasi-Biennial Oscillation through idealized large-ensemble experiments based on a global atmospheric model with a well-resolved stratosphere. Although culminating in autumn, the prescribed sea ice loss induces near-surface warming that persists into winter and deepens as the SSW develops. The resulting temperature contrasts foster a deep cyclonic circulation over the North Pacific, which elicits a strong upward wavenumber-2 activity into the stratosphere, reinforcing the climatological planetary wave pattern. While not affecting the SSW occurrence frequency, the amplified wave forcing in the stratosphere significantly increases the SSW duration and intensity, enhancing cold air outbreaks over the continents afterward.

INTRODUCTION

The extent of sea ice coverage over the Arctic Ocean has dramatically declined over the past few decades[1]. The anomalously warm Arctic surface associated with the Arctic sea ice loss has been linked to the mid-latitude surface cooling in the subsequent boreal winter[2–8]. Several studies have suggested that this linkage could involve the wintertime stratospheric circulation by enhancing the upward planetary wave (PW) activity and weakening the polar vortex[9–14]. Temperature anomalies induced by the vortex weakening could subsequently descend into the troposphere on time scales of weeks to months[15], potentially leading to cold air outbreaks (CAOs) over the continents[16,17]. Case studies based on observations[18] or model simulations[19] even suggested that the enhanced wave flux could be strong enough to cause the demise of the polar vortex associated with the sudden stratospheric warming (SSW) phenomenon.

However, the atmospheric response to Arctic sea ice loss remains a subject of much debate[20–24]. The effects of sea ice reduction on the atmospheric circulation and, in particular, on the warm Arctic-cold continent pattern at the surface have been attributed to internal variability[25–29] or to covarying sea surface temperature (SST) forcing outside of the Arctic[30]. Furthermore, the connection to the stratosphere appears sensitive to the geographical location of Arctic sea ice loss, leading to conflicting results. A numerical study[31] found polar vortex weakening in response to warm anomalies (representing sea ice loss) in the Barents-Kara Seas (Atlantic sector) and strengthening in response to anomalies in the Chukchi-Bering Seas (Pacific sector). Yet, a different numerical study[14] and observations[32] suggested that the sea ice loss over the Pacific sector is responsible for a weakened polar vortex.

Unraveling the exact dynamical mechanism linking the forced PW activity entering the stratosphere to the actual sea ice loss has been difficult. Previous studies inferred that the localized shallow heating due to sea ice reduction could modify the upward PW propagation from the troposphere into the stratosphere following changes in synoptic eddies and their feedback on the mid-latitude jet[32,33]. Yet, the complete chain of events is not fully understood. The relative importance of the autumn or winter sea ice loss has also remained unclear. A recent study found that the winter atmospheric circulation response to sea ice loss is primarily driven by sea ice loss in winter rather than in autumn[34]. Moreover, irrespective of the sea ice change, the polar stratosphere is influenced by the Quasi-Biennial Oscillation (QBO), the 11-year solar cycle, and the El Niño-Southern Oscillation (ENSO). As a 28-month oscillation of the stratospheric equatorial zonal wind[35], the QBO may affect the boreal polar vortex by altering the background flow through which PWs propagate into the stratosphere[36]. The SSW occurrence frequency tends to be higher during its easterly phase (EQBO) compared to its westerly phase (WQBO) regardless of the ENSO state[37]. The QBO may likewise modulate the stratospheric response to sea ice loss[38]. With roughly a 40-year record of high-quality atmospheric and sea ice data during the satellite era, observational analyses alone are unlikely to illuminate the connection between polar stratospheric variability, SSWs, and sea ice loss or its dependency on the QBO phase. While model simulations may help, the simulated QBO-SSW connection is weak compared to observations[39]. Often overlooked, the QBO's seasonal evolution from the period of sea ice loss (starting in June) through the following winter further obscures its role. Overall, the gaps in understanding the detailed mechanisms associating the surface processes and their subsequent impact on the stratosphere contribute to the uncertainties in distinguishing the potential sea ice-stratosphere connection from internal variability and other external forcings.

This paper attempts to elucidate the fundamental mechanisms linking the surface processes associated with sea ice loss to the wintertime stratospheric dynamics. Through large-member ensemble experiments using a climate model with a well-resolved stratosphere, the QBO is constrained to one phase throughout the winter. Given that SSWs occur more often during EQBO, we focus on the EQBO phase, which is also the more

---

[1]School of the Coastal Environment, Coastal Carolina University, South Carolina, SC, USA. [2]Norwegian Institute for Air Research, Kjeller, Norway. [3]Norwegian University of Science and Technology, Trondheim, Norway. [4]Faculty of Science, Niigata University, Niigata, Japan. ✉email: jzhang1@coastal.edu

npj

robustly represented and sustained phase of the QBO internally generated in the model. The effects of ENSO, the solar cycle, and global warming are all excluded from the experimental design. To avoid conflating the effects of sea ice loss in different sectors, this study focuses solely on the Pacific sector, where the observed August-September-October Arctic sea ice extent shows the strongest decline and covers the largest area of the Arctic Ocean in recent decades[40,41]. The atmospheric response to sea ice loss in that sector has received much less attention than over the Atlantic sector. Through carefully designed model simulations, the paper addresses how the autumnal sea ice loss over the Pacific sector impacts the most basic characteristics of SSWs.

As detailed below, the results indicate that this Pacific sector sea ice loss elicits enhanced near-surface upward wave propagation primarily over the Northwestern Pacific region and the increased PW forcing in the polar stratosphere. The latter tends to extend the SSW duration and strengthen the accompanying stratospheric wind reversal, with important consequences for the surface climate.

RESULTS

SSW characteristics in response to sea ice loss

Our results rely on contrasting 1-year-long (June–May) large-ensemble simulations with prescribed sea ice loss over the Pacific sector (denoted LOW) to those without (denoted CNTL). By construction, the difference (LOW-CNTL) reflects the response to sea ice loss. Composites of SSW events are made and diagnosed for atmospheric structures and wave forcing induced by sea ice loss. We focus on the EQBO since (i) SSWs tend to occur more frequently during the easterly phase and (ii) model biases and limitations limit our ability to evaluate the WQBO case. The Methods Section explains the experimental design and provides further details on why we do not consider the results relative to the WQBO phase.

Figure 1 summarizes the SSW characteristics in CNTL (gray) and LOW (red) during EQBO. The definitions are provided in the Methods Section. Most SSW onset dates are found between January and March (Supplementary Fig. 1), with the mean onset date being February 4 in CNTL and February 2 in LOW. The number of polar vortex splits relative to polar vortex
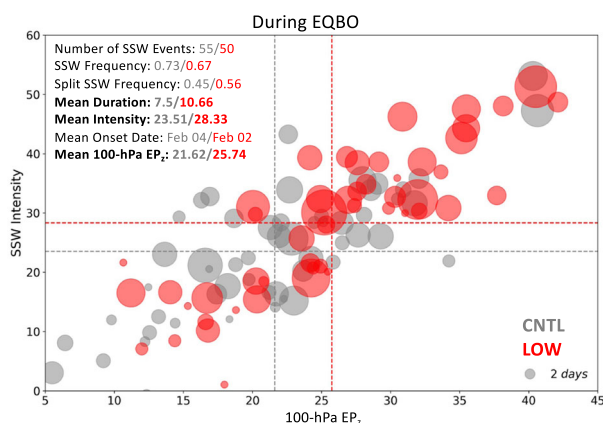

Fig. 1 Changes in SSW characteristics induced by Pacific-sector Arctic sea ice loss. Scatter plot of the 100-hPa EP_z (vertical EP Flux component) averaged between 45°N–75°N, 5 days prior to the onset (x-axis unit in $10^{-2}\,m^2\,s^{-2}$) versus SSW intensity (measured as a zonal-mean zonal wind deceleration, y-axis unit in $m\,s^{-1}$). Bubble size indicates the SSW duration in days, with a reference size provided. The mean values along each axis are shown as dashed lines. The split SSW frequency is the ratio of split SSW events to the total number of SSW events. Bold text indicates statistical significance at the 95% level.

displacements increases in LOW but not significantly. A linear relationship exists between the vertical Eliassen-Palm (EP) flux component (EP_z) at 100 hPa and the SSW intensity, as increasing upward wave propagation into the stratosphere further perturbs the polar vortex. Overall, the mean 100-hPa EP_z and SSW intensity, as well as the SSW duration are significantly larger in LOW (Supplementary Fig. 2). Hence, the autumnal sea ice loss over the Pacific sector leads to more persistent SSW events with stronger zonal-mean zonal wind reversals.

Composites of the geopotential height at SSW onset (day 0) are shown in Fig. 2 at 100 hPa (panels a, b) and 10 hPa (panels d, e) for CNTL, LOW, and their difference (i.e., the response in panels c, f). Line contours indicate the distorted polar vortex at the SSW onset. The filled contours represent departures from climatology, defined as the 31-day running average of the ensemble mean of all ensemble members in CNTL and LOW. Hereafter, the departures from climatology are referred to as anomalies. At 100 hPa, the polar vortex is displaced toward Northern Siberia. Significant trough deepening occurs in response to the prescribed sea ice loss (panel c). Specifically, the geopotential height is significantly lower from Eurasia to the Date Line, along with a localized negative height response over the North Atlantic. At 10 hPa, the polar vortex has tilted westward and is centered over Scandinavia, with large positive height anomalies over the polar cap. The polar vortex becomes more significantly displaced during SSW in response to the sea ice loss (panel f).

Enhanced upward PW propagation from the troposphere into the stratosphere generally accompanies SSW events[42]. As illustrated in Fig. 1, the mean upward wave flux prior to SSW onset becomes even more pronounced in response to sea ice loss. Figure 3 details the composite time evolution by the 100-hPa EP_z anomalies (averaged between 45°N and 75°N) in panels a, b, along with the vertical distribution of the zonal-mean zonal wind anomalies at 60°N in panels d, e. Prior to SSW onset (from day −20 to day 0), the anomalous upward wave activity increases, weakening the stratospheric zonal-mean zonal wind. Following the onset, the negative wind anomalies reach the surface within a few weeks, consistent with SSW-related observed characteristics[15,43]. The zonal wavenumber decomposition of EP_z reveals that the anomalous wavenumber 1 (WN1) dominates over wavenumber-2 (WN2) in the pre-onset period in both CNTL and LOW. The concurrent peaks of WN1 and WN2 greatly amplify the overall upward EP_z anomaly in LOW.

The sea ice loss elicits a strong response in the zonal wind reversal and upward wave propagation during SSWs (panels c, f), in support of Fig. 1. This response consists of a significantly stronger wind reversal in the extended period following onset that contributes to the aforementioned longer SSW duration. The stronger wind reversal follows a significantly enhanced upward PW activity between day −10 to day 0, initially by the WN2 component response. The persistence of significant and deep negative wind response to day 20 implies a stronger troposphere-stratosphere coupling in the presence of sea ice loss.

The upper panels of Fig. 4 depict the latitude-altitude sections of the EP flux (as vectors) and associated wave forcing (i.e., EP flux divergence as filled contours) for the CNTL, and the corresponding response to the prescribed sea ice loss averaged in the 10 days prior to onset. The remaining rows illustrate the corresponding WN1 and WN2 components. For SSW in CNTL, the anomalous wave activity propagates upward from the troposphere in the mid-latitudes, refracting more equatorward in the stratosphere. The anomalous wave forcing strongly decelerates the wind, weakening the polar vortex as expected prior to SSW. Comparing panels c, e reveals that WN1 contributes mainly to the anomalous upward activities and wave forcings, consistent with the 100-hPa EP_z results in Fig. 3a.

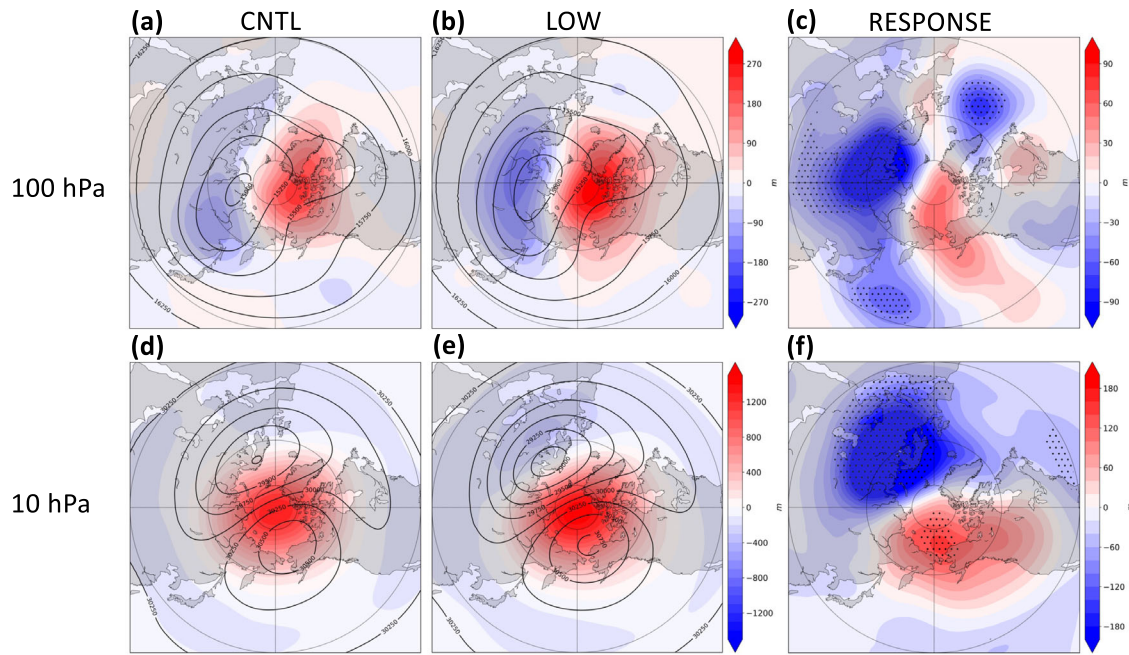As shown in Fig. 4b, the sea ice reduction enhances the upward wave propagation and the wave decelerative effects. The

Fig. 2 Changes in the polar vortex characteristics induced by Pacific-sector Arctic sea ice loss. Composite of the 100-hPa (**a**–**c**) and 10-hPa (**d**–**f**) geopotential height at SSW onset (day 0). The left column corresponds to the CNTL experiment, the middle column to the LOW experiment, and the right column to the response to sea ice loss (i.e., LOW-CNTL). Line and filled contours are total field and anomaly (defined as the departure from climatology), respectively, in (**a**, **b**, **d**, **e**). Stippling in (**c**, **f**) indicates statistical significance at the 95% level in the response.
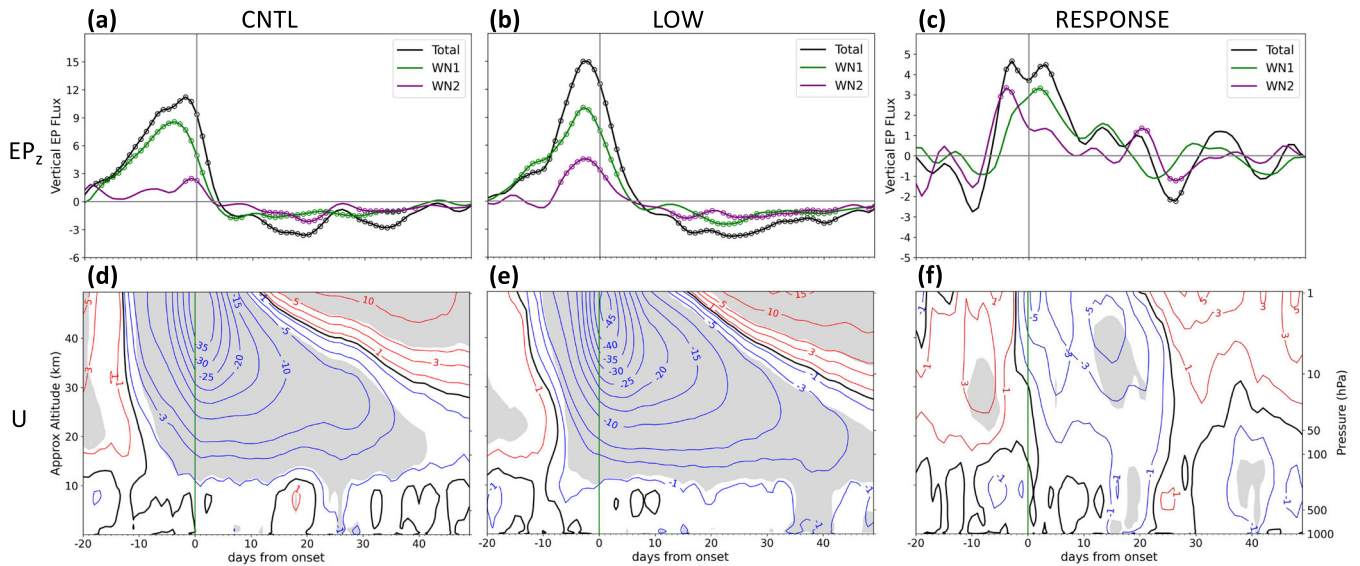

Fig. 3 Composite zonal-mean zonal wind (U) and vertical EP Flux component (EP$_z$) during SSW. The time series of 100-hPa EP$_z$ anomaly (averaged in 45°N–75°N), along with their decomposition in zonal wavenumbers 1 and 2 (**a**–**c**; in 10^{-2} m^2 s^{-2}), along with the time-height cross-section of 60°N U anomaly (**d**–**f**; in m s^{-1}). The left column corresponds to the CNTL experiment, the middle column LOW experiment, and the right column the response (i.e., LOW-CNTL). Open circles (**a**–**c**) and gray shading (**d**–**f**) indicate statistical significance at the 95% level.

increased wave-activity response originates from the near-surface and becomes concentrated toward higher latitudes in the stratosphere. The associated zonal-mean zonal wind response shows that the subtropical jet intensifies and that the mid-latitude flank of the polar night jet becomes stronger. An enhanced polar night jet acts as a more effective waveguide, steering the upward wave activity toward higher latitudes. The stronger wave forcing further weakens the polar vortex compared to CNTL, leading to more intense and persistent SSW events (as noted in Figs. 1, 3).

Above 100 hPa, both WN1 and WN2 responses are large. However, throughout the troposphere, the upward wave-activity response arises mainly from WN2 between 40°N and 60°N (vectors in panel f).

Near-surface upward wave activity
To identify the upward wave-activity response in the troposphere arising essentially from WN2, we examine the global distribution of the eddy heat flux at 850 hPa during the 10-day period before
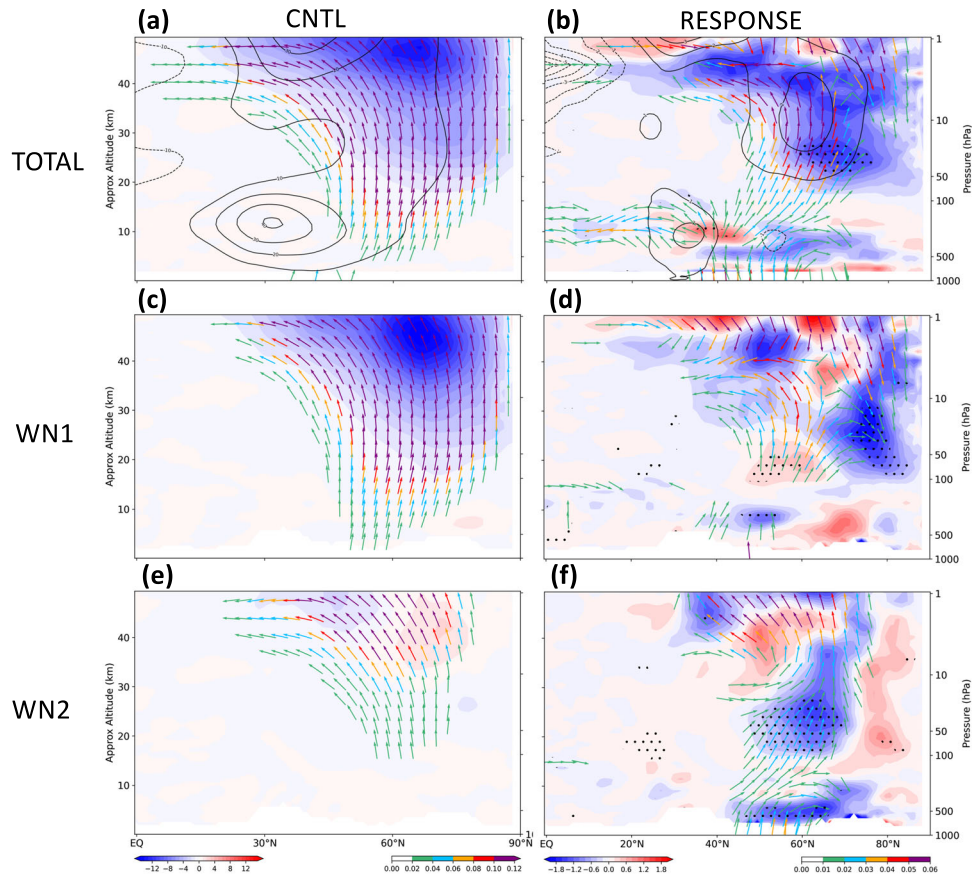
Fig. 4   Planetary wave EP flux. Zonal-mean zonal wind (line contours; in m s^{-1}), EP Flux anomaly (vector; in m^2 s^{-2}), and divergence anomaly (filled contours; in m s^{-1} day^{-1}) in CNTL (left column), and response (right column) for all wavenumbers (**a–b**), WN1 (**c–d**), and WN2 (**e–f**) averaged from day -10 to day -1 prior the onset. Stippling indicates statistically significant regions of divergence (filled contours in **b**, **d**, **f**) at the 95% level.
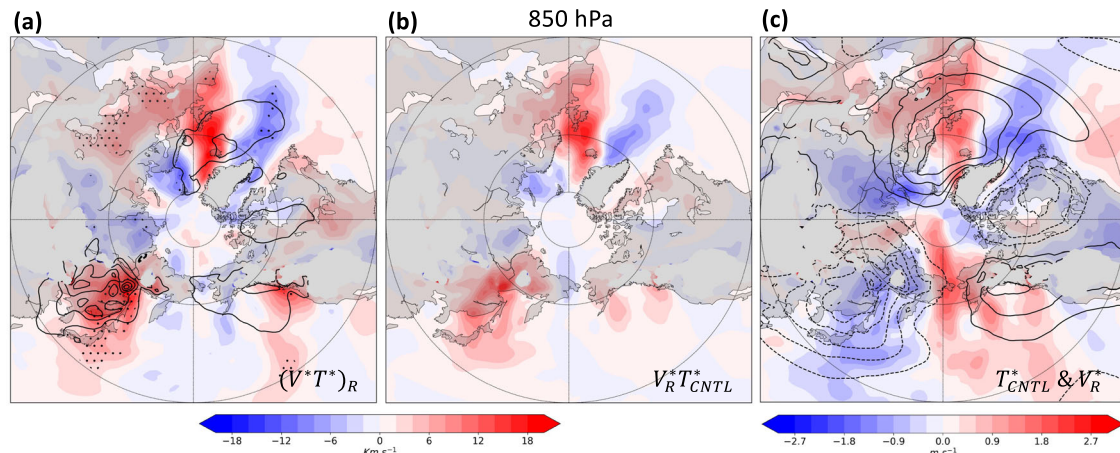

Fig. 5   Components of poleward eddy heat flux. Poleward eddy heat flux in CNTL (line) and its response (R) to sea ice forcing (filled) (**a**) and decomposed poleward eddy heat flux $V_R^* T_{CNTL}^*$ in (**b**). The underlying eddy fields of T_{CNTL}^* (line; in K) and V_R^* (filled; in m s^{-1}) are in (**c**) at 850 hPa. All variables are averaged from day -10 to day -1 prior to the onset. The line contour interval is 20 K m s^{-1} in (**a**) and 2 K in (**c**). Stippling in (**a**) indicates statistical significance at the 95% level.

the SSW onset. As a product between the eddy meridional wind and eddy temperature fields (i.e., V^*T^*), the meridional eddy heat flux is proportional to the local vertical wave activity. A positive (i.e., poleward) eddy heat flux corresponds to local upward wave activity. Fig. 5a shows the CNTL eddy heat flux as line contours and the eddy heat flux response to the sea ice loss, $(V^*T^*)_R$, as filled

contours. Before the SSW onset, the CNTL poleward eddy heat flux is most dominant over the Northwestern Pacific between 40°N and 60°N. The imposed sea ice loss significantly enhances this dominant heat flux region, leading to an enhanced upward wave activity over the Northwestern Pacific near 130°E (panel a). Along the 60-degree latitude circle, other weaker patches of CNTL
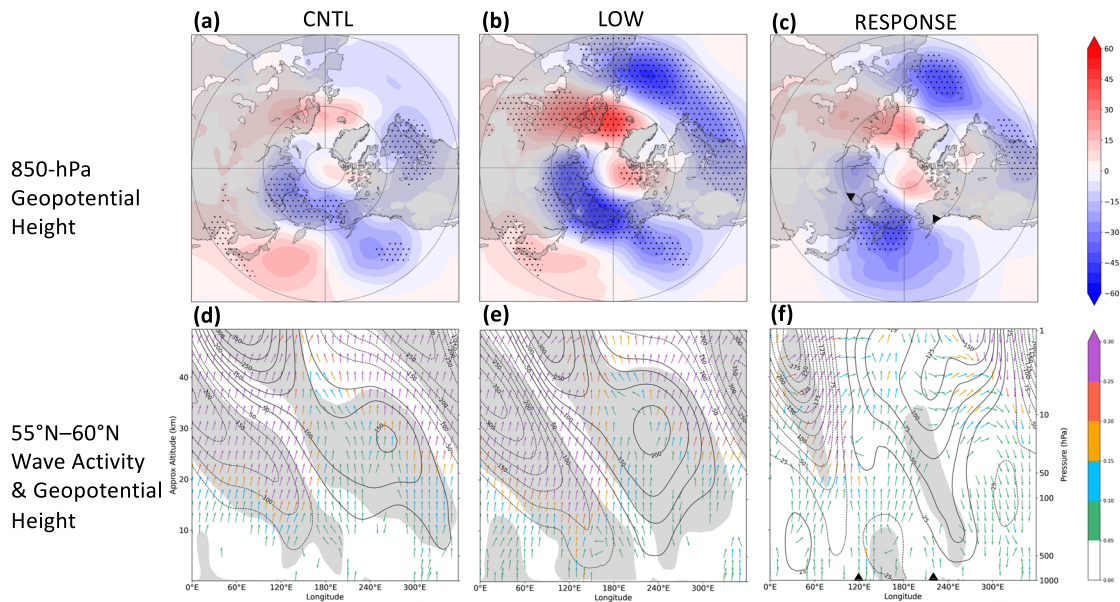
Fig. 6 Composite geopotential height and wave activity flux. 850-hPa longitude-latitude cross-section of geopotential height anomaly in CNTL (**a**), LOW (**b**), and response (**c**), 55°N–60°N longitude-height cross-section of the eddy component of geopotential height anomalies (contours; in m) and wave activity flux anomaly (vector; in m^2 s^{-2}) in CNTL (**d**), LOW (**e**), and response (**f**) averaged from day -10 to day -1 prior the onset. Stippling and shading indicate statistical significance at the 95% level. The black triangles mark the longitudinal edges of the sea ice loss region.

poleward eddy heat flux exist over the Euro-Atlantic and North American regions. The Euro-Atlantic patch near the Greenwich Meridian also becomes strongly enhanced due to $(V^*T^*)_R$ that extends eastward well in Central Europe. Supplementary Fig. 3 confirms the response in local upward wave activity (line contours) over these regions. When zonally averaged, the associated $(V^*T^*)_R$ contributes largely to the near-surface upward EP flux response in Fig. 4b.

To relate the wind and temperature responses to the region of enhanced upward wave activity, we decompose $(V^*T^*)_R$ into its linear and nonlinear components[44,45], as described in Eq. 1 in the Methods Section. The decomposition reveals that the amplified upward wave activity response arises mainly from the linear term $V^*_R T^*_{CNTL}$ (compare panels a, b). Supplementary Figure 4 details the time evolution of each component, confirming the predominance of this particular term prior to the onset. Over the Northwestern Pacific, the enhanced upward wave activity peaks at day -6 from the coupling between the CNTL cold temperature and southward wind response. Over the Euro-Atlantic region (panel c), the coupling between the CNTL warm temperature and northward wind response produces the strong total eddy heat flux response about 5 days later (day -1), which is consistent with a downstream propagation of wave activity seen in Supplementary Fig. 3 and ultimately the amplification of the WN2.

The upper panel of Fig. 6 shows the 850-hPa geopotential height. For CNTL, significant cyclonic anomalies appear over Northeastern Eurasia and the North Pacific as well as over Eastern Canada (panel a). Similar patterns of height anomalies are found to be precursors of SSW events[46,47]. The prescribed sea ice loss greatly strengthens these cyclonic anomalies around the 60-degree latitude circle (panel b), resulting in the cyclonic response over the North Pacific (panel c). The circulation around this cyclonic response produces a southward flow near 130°E, consistent with Fig. 5c, responsible for the enhanced $(V^*T^*)_R$ over the Northwestern Pacific region. This circulation likewise produces a northward flow near the Date Line that could bring warmer-wetter air poleward from the lower latitudes. The prescribed sea ice loss also strengthens the anticyclonic anomalies over Northeastern Eurasia, leading to an anticyclonic response within the

Arctic circle between Greenland and Scandinavia. The associated northward flow response near the Greenwich Meridian (shown in Fig. 5c) is responsible for the enhanced $(V^*T^*)_R$ over the Euro-Atlantic region (Fig. 5a). The overall 850-hPa height response has a large WN2 component.

The longitude-altitude structure of the eddy geopotential height prior to the SSW onset is illustrated in the lower panels of Fig. 6, along with the wave activity vectors. This structure is averaged between 55°N and 60°N, covering the region of strong upward wave activity (Fig. 5a). Below 500 hPa, the geopotential height anomalies and responses exhibit a relatively weak phase tilt with altitude, suggesting a barotropic structure in the lower troposphere. Indeed, the height anomalies and the responses at 850 hPa are roughly similar to those at 500 hPa (shown in Supplementary Fig. 5). Panel f clearly shows the WN2 characteristic in the height response throughout the troposphere, with a significant cyclonic response between 130°E and 180°E and anticyclonic response around 0°E with upward wave activity, consistent with the strong $(V^*T^*)_R$ region at 850 hPa (Fig. 5a). In the stratosphere, the height anomalies have a pronounced westward tilt, associated with stronger wave activity flux at these altitudes prior to SSW (Fig. 4).

Mechanism for the cyclonic response over the North Pacific

To understand the cyclonic response responsible for the enhanced $(V^*T^*)_R$ over the Northwestern Pacific, we examine the tropospheric temperature and meridional wind structures prior to SSW onset. In Fig. 7, the filled contours show the temperature anomalies in CNTL and LOW and the temperature response (T_R). At high latitudes (averaged between 60°N and 80°N), the longitude-altitude temperature distribution in CNTL indicates anomalous cooling westward of 190°E mainly below 7 km, with an overlying warm layer eastward of 170°E (panel a). In LOW, near-surface warm anomalies appear between 180°E and 240°E, consistent with the anticipated effect of sea ice loss and extending upward toward the overlying warm layer (panel b). Averaged between 150°E and 210°E, the latitude-altitude temperature distribution (lower panel) reveals the upward extension of warm
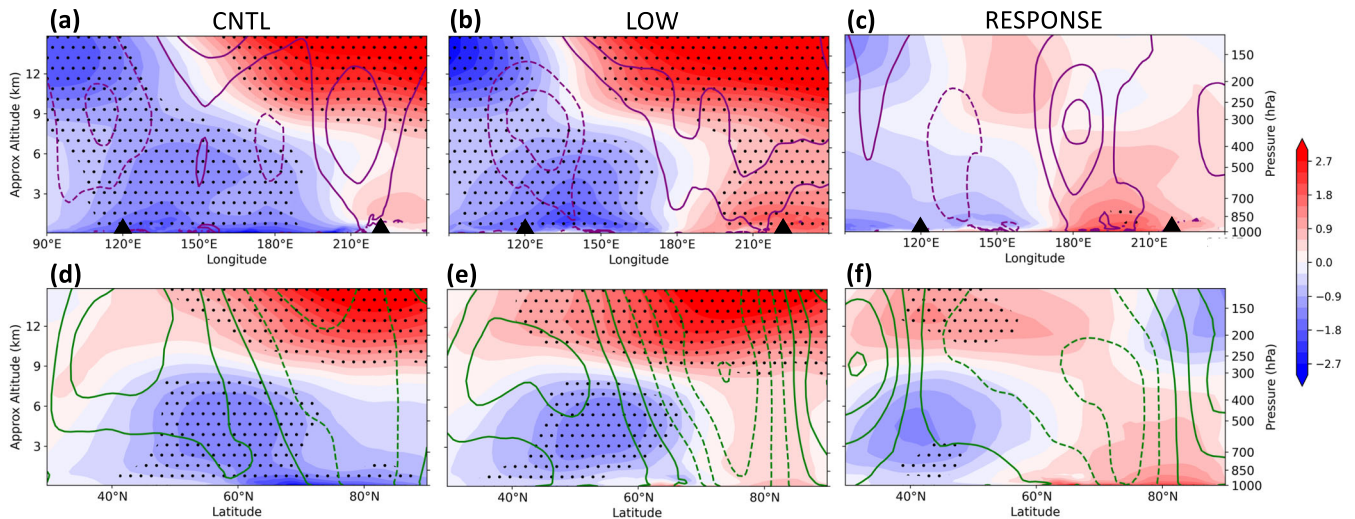
Fig. 7 Composite temperature (T), zonal wind (U), and meridional wind (V) prior to SSW (averaged between day −10 to day −1). Longitude-altitude cross-section of T and V anomaly in CNTL (**a**), LOW (**b**), and the response (**c**). T (averaged between 60°N–80°N) is shown as filled contours and V at 60°N as line contours (every 1 m s^{-1} interval). The black triangles mark the longitudinal edges of the sea ice loss region. Corresponding latitude-altitude cross-sections of T and U anomaly (averaged over 150°E–210°E) are given in (**d–f**). Stippling indicates T statistical significance at the 95% level.
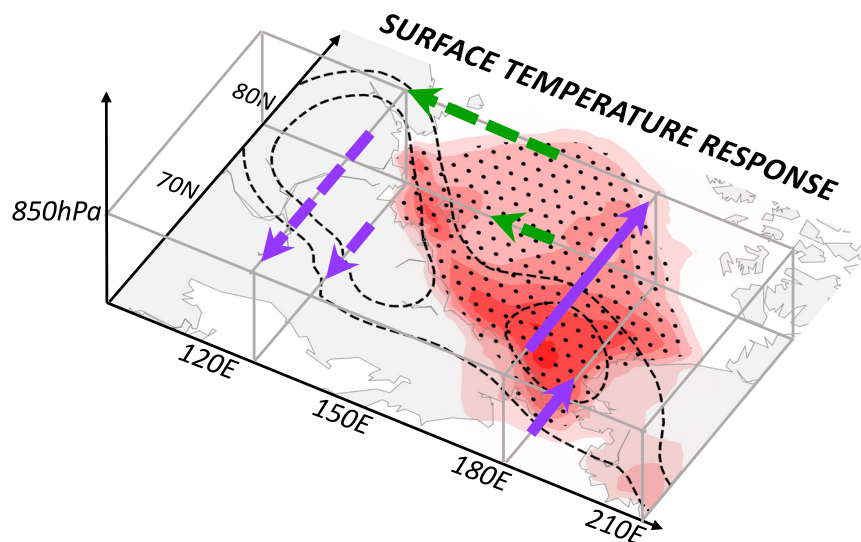

Fig. 8 The mechanisms associated with sea ice loss. A schematic of the wind response at the surface (short arrows) and 850 hPa (long arrows) in colors and styles shown in Fig. 7c, f, along with the CNTL 850-hPa geopotential height anomaly as line contours (given at −23 m and −20 m; same as filled contours in Fig. 6a) and surface temperature response as filled contours (every 1 K interval).

anomalies in LOW poleward of 70°N. Hence, the high latitude warming response to the prescribed sea ice loss near the Date Line deepens as the SSW develops, extending well into the lower troposphere (panels c, f). Additionally, a cooling response occurs at high latitudes west of the Date Line and at mid-latitudes south of 60°N, due to cold air advection on the western flank of the cyclonic anomaly (not shown).

The existence of zonal and meridional temperature gradients along the lower boundary implies the existence of vertical shear of the horizontal winds through the thermal wind balance (see Eq. 2 in the Methods Section). These horizontal winds drive the anomalous wave activity fluxes. Line contours in Fig. 7 correspond to the meridional wind (V) and zonal wind (U) in purple and green, respectively. The warming response triggers a significant northward flow response (V_R). At about the Date Line, the positive vertical shear in V_R is consistent with the eastward temperature gradient (panel c). At about 130°E, the negative vertical shear in V_R

coincides with the westward temperature gradient. The induced warming also elicits a strong westward flow response (U_R; panel f). This negative vertical shear structure of U_R is above the warming response where the underlying temperature gradient in the northward direction is positive. As summarized in Fig. 8, the near-surface warming response (shown as filled contours) results in a deep cyclonic response over the North Pacific (illustrated by wind arrows with color and line styles shown in Fig. 7) that intensifies the height anomaly precursory to SSWs (dash contours).

Planetary wave interference

To assess the tropospheric precursors to SSWs, linear stationary wave interference theory has been used in past studies[44,48]. When the forced response is in-phase (out-of-phase) with the climatological PW pattern in the troposphere, upward wave propagation from the troposphere to the stratosphere is enhanced
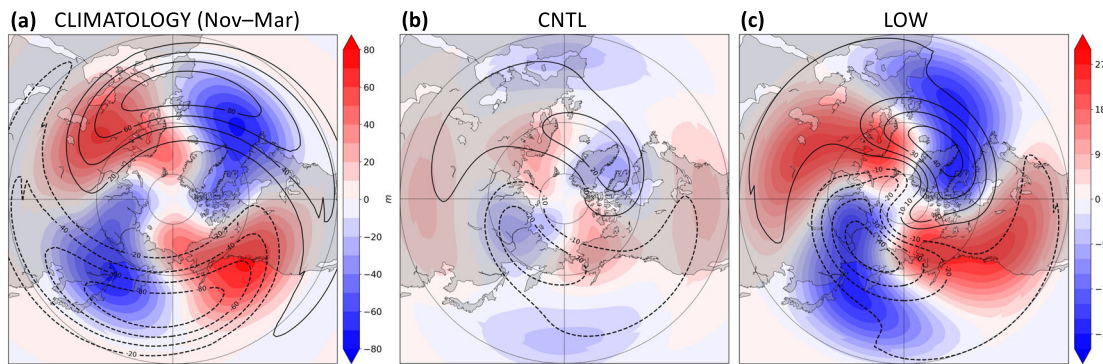
Fig. 9 Planetary wave interference. WN1 (line contours) and WN2 (filled contours) components of the 500-hPa geopotential height (m) for November–March mean climatology (**a**) and composite anomalies averaged from day −10 to day −1 prior to the onset in CNTL (**b**) and LOW (**c**).

(suppressed). The left column of Fig. 9 shows the climatological WN1 (line contours) and WN2 (filled contours) components of the extended wintertime 500-hPa geopotential height. The corresponding anomalous field in CNTL and LOW are illustrated in the remaining columns. For SSW events in CNTL, the anomalous WN1 and WN2 patterns tend to be in-phase with climatological wave patterns, albeit the patterns are now shifted poleward for SSW. The positive and negative geopotential height of the WN1 pattern at around 60°N correspond to the deep anticyclonic and cyclonic anomalies identified in Fig. 6a and Supplementary Fig. 5a. The wave structures in LOW are similar to those in CNTL, but the amplitudes are much larger, especially for WN2 which has more than doubled. Moreover, the wave fields are extending further equatorward. Thus, the warming caused by sea ice loss intensifies both the WN1 and WN2 components of the climatological geopotential height field in the troposphere, enhancing the vertical wave flux in the troposphere and lower stratosphere (as seen in Figs. 3f, 4b, 5a, 6f).

Composite of SSW event in reanalysis data

To affirm model results, we examine SSW composites in the JRA-55 re-analyses[49]. Years with low (high) autumnal Arctic sea ice are identified when the standardized, detrended Pacific-sector Arctic sea ice concentration (SIC) values averaged in September are less (more) than zero. The observed declining SIC trend is removed using the Empirical Mode Decomposition. Between 1979–2021, 16 SSW events (among a total of 27) occurred when an EQBO phase prevailed over the 30 days prior to SSW onset. The characteristics of these 16 SSWs are shown in Supplementary Fig. 6, in terms of 100-hPa EP$_z$, intensity, and duration, as was done in Fig. 1, and in terms of composited zonal wind cross-sections, as was done in Fig. 3. For low autumnal sea ice years, the SSW events tend to be of longer duration, more intense, and are associated with larger upward wave flux. Given such few observed events, the changes in the SSW characteristics are not statistically significant. Furthermore, the SSW characteristics in the observational records are influenced by several factors mentioned in the Introduction; nevertheless, the general response in SSW characteristics due to Pacific sector sea ice loss under the EQBO bears some similarity to the model results shown in Figs. 1, 3.

Cold air outbreaks

We end by highlighting the importance of the Pacific sector sea ice loss and the associated SSW impact on cold air outbreaks. Figure 10 shows the surface temperature response following the onset of SSWs. Consistent with the more intense and prolonged SSW, a reinforced bias toward the negative Arctic Oscillation phase following the onset leads to more intense CAOs over Eurasia and North America in the presence of sea ice loss.
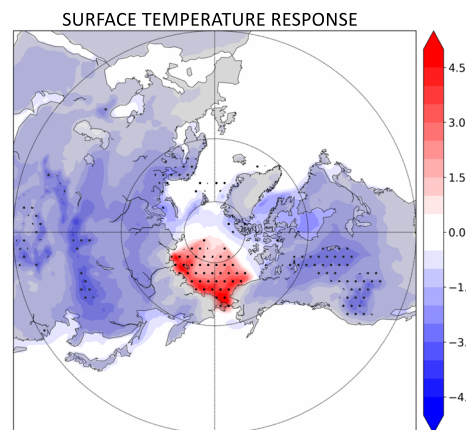

Fig. 10 Intensified cold air outbreaks induced by Pacific-sector Arctic sea ice loss following the onset. Composite of the surface temperature (K) response (CNTL-LOW) averaged from day 0 to day +30 after the onset. Stippling indicates statistical significance at the 95% level.

DISCUSSION

Projections about the potential changes in SSWs resulting from climate change have largely focused on the frequency of SSW occurrence. There is disagreement in the current literature[50–52], which could reflect opposing Arctic stratosphere model responses to different aspects of climate change. Through idealized climate model experiments that exclude the effects of ENSO, solar activity, global warming, and ozone loss, we provide supporting evidence that autumnal sea ice loss over the Chukchi-Bering Seas (i.e., the Pacific sector) modifies the characteristics of SSWs rather than altering their frequency of occurrence. Namely, the enhanced upward wave activities (especially, those from WN2) and associated stronger westward deceleration in the stratosphere significantly extend the SSW duration and strengthens the stratospheric wind reversal. Following SSW onset, more intense CAOs are induced over Eurasia and North America in the presence of sea ice loss. Since there is no continental cooling in the seasonal surface air temperature response (panels a–d in Supplementary Fig. 7), this implies that CAOs are induced by a more persistent and stronger SSW instead of by mean state difference.

Through poleward heat flux decomposition, we demonstrate that the interaction of the sea ice loss with a precursory cyclonic anomaly over the North Pacific during the pre-onset stage of SSW is the critical factor in amplifying the near-surface wave-activity response (especially, over the Northwestern Pacific region), despite the seasonal-mean thermal response to the sea ice being

shallow (Supplementary Fig. 7). The seasonal timing (i.e., autumn or winter) of the sea ice anomaly appears less relevant. The circulation of this cyclonic response is in thermal wind balance with the warming induced by sea ice loss that extends into the lower troposphere and enhances the height anomalies before SSW onset.

The model response to sea ice loss includes increased wave activity across North America. The amplified near-surface response of upward wave activity near the Northwestern Pacific region induces a downstream wave activity across North America and into Eastern Europe, as suggested by zonal vectors in Supplementary Fig. 3. This downstream response leads to an increasingly WN2 characteristic in the geopotential height response and the amplified upward wave activity response of the Euro-Atlantic region that appears 5 days after the response over the Northwestern Pacific region, as evident in Supplementary Fig. 4. The greatly intensified WN2 components of the climatological 500-hPa geopotential height field and the WN2 vertical wave flux response in the troposphere may be associated with this downstream propagation.

The presented geopotential height and surface cooling patterns (Figs. 6b, 10) are similar to another numerical model result[53] that forced sea ice loss over the Chukchi-Bering sea (see their Supplementary Fig. 13). Although these authors argued that sea ice loss over the Pacific sector has little impact on the stratospheric polar vortex stretching, it does seem to influence the characteristics of SSW events in our model. Given the expected reduction of Arctic sea ice in a warmer future climate (especially, in the Pacific sector), the future SSW characteristics could result in more extreme wintertime CAOs over continental areas. Hence, the autumnal sea ice may be regarded as a precursory factor for extreme weather events in the following winter.

These relationships between autumnal Arctic sea ice loss over the Pacific sector and SSW events may be model-dependent (e.g., regarding the inclusion of the stratosphere or the QBO) and forcing-dependent (e.g., how exactly the sea ice forcing is specified). As noted in the Introduction, various models and setups have been employed to understand the impact of sea ice loss on the stratosphere.

A two standard deviation of sea ice loss over the Pacific sector is used to prescribe the anomalous low sea ice condition. We acknowledge that our prescription corresponds to a very low sea ice cover, but this condition has occurred more frequently with global warming. In recent years, autumnal sea ice over the Pacific sector has declined significantly and has regularly fallen outside of two standard deviations. As found in previous studies[10,31], the magnitude of sea ice loss could impact the polar vortex response and, in our case, SSW characteristics.

The EQBO phase may nevertheless play an important role in our results, in that it favors geopotential anomalies in the lower troposphere that projects on precursors of SSWs. An important pathway of troposphere-stratosphere coupling by which the QBO phase influences tropical convection patterns and ultimately enhances upward PW propagation in the stratosphere was identified[54]. Supplementary Fig. 5d shows the 500-hPa geopotential height difference between the two QBO phases in the CNTL simulation. The results are shown for November when the tropospheric pathway of the QBO's impact is strongest[54], but similar anomalies are apparent throughout the extended winter. We note that, in CNTL, the key precursory cyclonic patterns (identified over Eastern Eurasia and the North Pacific) are enhanced in EQBO compared to WQBO, implying that the background state, conditioned by the QBO, may influence the response of SSWs to the sea ice loss. While difficult, differentiating the QBO phases (whether in numerical experiment setup or in composite based on models/observational results) may be

important in understanding the stratospheric response to sea ice loss.

In summary, we demonstrate that, during EQBO, autumnal sea ice loss over the Chukchi-Bering Seas modifies the characteristics of SSWs by increasing their duration and intensity, yet without necessarily altering their frequency of occurrence. The results are based on idealized climate model experiments that exclude the effects of ENSO, solar activity, global warming, and ozone loss. Under these conditions, the near-surface warming induced by the sea ice loss persists into winter and deepens as the SSW develops. The resulting temperature contrasts foster a deep cyclonic circulation over the North Pacific that elicits an enhancement of WN2 upward wave activities into the polar stratosphere, which extends the SSW duration and strengthens the stratospheric wind reversal. Consistent with the stronger and prolonged SSWs, CAOs become intensified over Eurasia and North America following the SSW onset, with potentially strong societal impact. Knowing the state of autumnal Arctic sea ice loss could then improve the long-range prediction of the wintertime CAOs over those continents.

METHODS

Model
The numerical experiments are performed using the National Center for Atmospheric Research (NCAR) Whole Atmosphere Community Climate Model version 6 (WACCM6), a global chemistry-climate model that is part of the NCAR Community Earth System Model version 2 framework[55]. Configured as an atmosphere-only component spanning the surface to the lower thermosphere, WACCM6 has improved stratospheric variability, including an internally generated QBO and realistic SSW climatology[55,56]. WACCM6's characterizations of the global atmospheric circulation are realistic, without notable model bias in the vortex region (Supplementary Fig. 8). Momentum deposition from vertically propagating gravity waves (generated by orography, fronts, and convection) is included in the model.

Experimental setup
Natural external forcings such as solar radiative variations associated with the 11-year solar cycle and volcanic eruptions can influence the stratosphere. Anthropogenic factors leading to global warming and ozone loss may, in principle, affect the SSW characteristics[57,58]. To avoid these impacts, which may mask the underlying mechanisms associated with sea ice loss, all experiments are based on gases and aerosols specified with respect to the pre-industrial control emissions according to the Coupled Model Inter-comparison Project Phase 6. Furthermore, a forcing corresponding to the solar minimum conditions is prescribed. Based on the historical time series of 10.7-cm solar radio flux (F10.7), the minimum solar forcing years are defined when F10.7 is less than 73 solar flux units. All variables related to solar forcing and geomagnetic activity are averaged during those minimum solar forcing years.

With a resolution of 0.95° latitude by 1.25° longitude, the model is initialized on 1 January 1850 and forced with the boundary conditions of an annually repeating daily climatology of sea surface temperature (SST) and sea ice concentration (SIC) from the historical time series data of the Hadley Centre. As such, interannual signals associated with ENSO are removed. After 10 years of integration, roughly four QBO cycles are internally generated with EQBO persisting throughout the 1858–1859 boreal winter.

The 1 June 1857 model state serves as a branching point for two simulations (Supplementary Fig. 9). For the control simulation, the model is allowed to continue with the aforementioned climatological SST and SIC boundary conditions for an additional year of spin-up before starting the control ensemble runs

(hereafter, CNTL). For the perturbed simulation, new SIC and SST boundary conditions are introduced. For SIC, the sea ice loss is specified in the Pacific sector, defined between 120°E–220°E and 65°N–90°N. In this sector, two standard deviation values are subtracted relative to climatology at each ice-covered grid box to represent sea ice loss. The SST values are empirically adjusted based on SIC[59]. We note that sea ice thickness is constant in the model and is 2 m in the Arctic. The regional sea ice loss is greatest in autumn, as the SIC differences in Supplementary Fig. 7 demonstrate. Like the control simulation, the perturbed simulation is spun-up for 1 year before starting the low sea ice ensemble runs (hereafter, LOW). The 1-year spin-up removes possible inconsistencies from the introduced boundary conditions, helping the model to attain a balanced state[31].

Thus, both ensemble experiments begin on 1 June 1858, when the initial temperature fields are randomly perturbated by order 10^{-14} K[60]. An ensemble size of at least 50 members is desirable[61]. Given the available computing resources, we performed 75-member ensembles of 1-year simulations.

The stable QBO phase during the 1858–1859 boreal winter is crucial to allow the experiments to elucidate how SSW respond to autumn sea ice loss during EQBO. Panel (a) of Supplementary Fig. 10 illustrates the 1-year QBO evolution for all CNTL and LOW members. The illustrated time series is defined as the zonal-mean zonal wind averaged over 5°S–5°N, 50–30 hPa. Overall, EQBO is persistent and similar between CNTL and LOW. The initial QBO is also similar on 1 June 1858, suggesting the absence of notable wind drift during the 1-year spin-up prior to the ensemble experiment.

The difference in the background stratospheric state at high winter latitudes between CNTL and LOW may potentially impact SSW, irrespective of the wintertime influence induced by autumn sea ice loss. However, this does not appear to be the case. As represented by the 10-hPa zonal-mean zonal wind at 60 °N (Supplementary Fig. 10b–d), the overall seasonal evolution of this mean state for all members in both CNTL and LOW is very similar, being nearly identical in summer and early autumn and exhibiting only small week-to-week wintertime variability due to the different timing of SSWs. Rather, it is the surface response due to the prescribed sea ice difference between CNTL and LOW that results in the variations of SSW characteristics.

Data analysis
The daily climatology is defined as the 31-day running average of the ensemble mean of all ensemble members in CNTL and LOW. Daily anomalies are calculated as deviations from that daily climatology. The SSW response (defined below) to the prescribed Arctic Pacific-sector sea ice loss is obtained by subtracting CNTL from LOW after compositing SSW events (i.e., the LOW-CNTL difference).

SSW definition and significance
Following the World Meteorological Organization convention, an SSW event is identified when the daily 10-hPa zonal-mean zonal wind at 60°N becomes easterly and the 10-hPa zonal-mean temperature difference between 50°N–70°N and 70°N–90°N is positive during November–March. Two events must be separated by at least 20 days of westerly winds[62]. To exclude the final warmings, the 10-hPa zonal-mean zonal wind 60°N must become westerly at least 10 days before April 30. The SSW onset date is the first day of the wind reversal. CNTL produces 55 SSW events with an annual occurrence frequency of 0.73, which is higher than 0.62 in observations[62]. LOW produces 50 SSW events with a slightly lower frequency. Once the SSW events are identified, composites are generated by averaging each event centered at the onset. The SSW occurrence frequency is defined as the number of SSW events divided by ensemble members. The SSW duration is

calculated from the number of consecutive days that the 10-hPa zonal-mean zonal wind at 60°N is easterly[63]. The SSW intensity is based on wind deceleration, which is defined as the difference in the zonal-mean zonal wind at 60°N and 10-hPa, 15–5 days prior to the onset date minus 0–5 days after the onset date[63]. The classification of SSW type is based on the geopotential height amplitude of zonal WN1 and WN2 averaged over 55°N-65°N at 10 hPa[64]. All the variables are tested using the bootstrap technique with replacement. Statistical significance is at the 95% level.

Eddy heat flux decomposition
The meridional eddy heat flux is an indicator of upward PW propagation. The LOW-CNTL difference in the total eddy heat flux, $[V^*T^*]_R$, can be decomposed into its linear and nonlinear components[44,45] as:

$$[V^*T^*]_R = [V^*_{CNTL}T^*_R + V^*_R T^*_{CNTL}] + [V^*_R T^*_R]_R \qquad (1)$$

Here, V and T represent the meridional wind and temperature field, respectively. The brackets indicate the composite average, and the asterisk next to a field denotes its departure from the zonal-mean. The subscript R represents the response to sea ice loss (i.e., LOW-CNTL). The first two terms on the right-hand side correspond to the heat fluxes due to the linear eddy interaction between the CNTL and response; the third term is the nonlinear eddy interaction due to the response. Each term is calculated throughout the SSW lifecycle[44].

Wave activities
To diagnose wave propagation and its forcing of the zonal-mean flow, the Eliassen-Palm (EP) flux and its divergence are computed[65]. The EP flux is parallel to the local group velocity, and its divergence can accelerate the zonal flow. The WN1 and WN2 components of EP flux is also analyzed to focus on the PW activity. Since PWs can propagate zonally, three-dimensional stationary wave activity fluxes are also calculated[66].

Thermal wind
The geostrophic balance between pressure gradient and Coriolis forces, combined with the hydrostatic equation leads to the thermal wind relationship[67].

$$\frac{\partial U}{\partial z} = -\frac{g}{fT}\frac{\partial T}{\partial y}$$
$$\frac{\partial V}{\partial z} = \frac{g}{fT}\frac{\partial T}{\partial x} \qquad (2)$$

Here, U represents the zonal wind, g gravity, f the Coriolis parameter, and x, y, z are zonal, meridional, and vertical directions, respectively.

Westerly QBO
To isolate the QBO influence, our experiment setup focuses strictly on EQBO persisting during the entire winter. Alternatively, analogous experiments were performed for WQBO. However, the results are not provided due to various problems. First, the QBO amplitude in WACCM6 is weak, and the WQBO pattern does not extend low enough into the lower stratosphere as compared to observations[55]. Furthermore, during late winter, notable WQBO "hiccups" occur in both CNTL and LOW experiments, with the attendant eastward equatorial wind becoming unstable and reduced to the point of nearly reversing (Supplementary Fig. 10c)—analogous to the observed WQBO during the 2015–2016 winter[68]. Such hiccup tendencies might contribute to an increased frequency of SSW occurrence. Finally, during the 1-year model spin-up, the equatorial wind tends to evolve quite differently between CNTL and LOW for the WQBO phase, leading to markedly different initial equatorial conditions when perturbations are

introduced in the ensemble experiment (as shown in Supplementary Fig. 9). As such, the comparison between the CNTL and LOW might be problematic. In most studies of the sea ice atmospheric response (except one[38]), the impact of separate QBO phases is not considered, and the reported results are inferred for the combined QBO phases.

DATA AVAILABILITY

The WACCM simulation data used in this study are available from the corresponding author upon reasonable request. The JRA-55 data set was provided by the Japan Meteorological Agency (https://jra.kishou.go.jp/JRA-55/index_en.html).

CODE AVAILABILITY

All codes used for analyses of the simulation data are available from the corresponding author upon reasonable request.

REFERENCES

1. National Snow and Ice Data Center. Arctic sea ice news and analysis: yearly archives. http://nsidc.org/arcticseaicenews/2016/ (2016).
2. Honda, M., Inoue, J., & Yamane, S. Influence of low Arctic sea-ice minima on anomalously cold Eurasian winters. *Geophys. Res. Lett.* **36** (2009).
3. Mori, M., Watanabe, M., Shiogama, H., Inoue, J. & Kimoto, M. Robust Arctic sea-ice influence on the frequent Eurasian cold winters in past decades. *Nat. Geosci.* **7**, 869–873 (2014).
4. Kug, J. S. et al. Two distinct influences of Arctic warming on cold winters over North America and East Asia. *Nat. Geosci.* **8**, 759–762 (2015).
5. Cohen, J., Pfeiffer, K. & Francis, J. A. Warm Arctic episodes linked with increased frequency of extreme winter weather in the United States. *Nat. Commun.* **9**, 1–12 (2018).
6. Mori, M., Kosaka, Y., Watanabe, M., Nakamura, H. & Kimoto, M. A reconciled estimate of the influence of Arctic sea-ice loss on recent Eurasian cooling. *Nat. Clim. Change* **9**, 123–129 (2019).
7. Tachibana, Y., Komatsu, K. K., Alexeev, V. A., Cai, L. & Ando, Y. Warm hole in Pacific Arctic sea ice cover forced mid-latitude Northern Hemisphere cooling during winter 2017–18. *Sci. Rep.* **9**, 1–12 (2019).
8. Kim, H. J. & Son, S. W. Recent Eurasian winter temperature change and its association with Arctic sea-ice loss. *Polar Res.* **39** (2020).
9. Kim, B. M. et al. Weakening of the stratospheric polar vortex by Arctic sea-ice loss. *Nat. Commun.* **5**, 1–8 (2014).
10. Sun, L., Deser, C. & Tomas, R. A. Mechanisms of stratospheric and tropospheric circulation response to projected Arctic sea ice loss. *J. Clim.* **28**, 7824–7845 (2015).
11. Nakamura, T. et al. The stratospheric pathway for Arctic impacts on midlatitude climate. *Geophys. Res. Lett.* **43**, 3494–3501 (2016).
12. Zhang, P. et al. A stratospheric pathway linking a colder Siberia to Barents-Kara Sea sea ice loss. *Sci. Adv.* **4** (2018).
13. Hoshi, K. et al. Weak stratospheric polar vortex events modulated by the Arctic sea-ice loss. *J. Geophys. Res. Atmos.* **124**, 858–869 (2019).
14. Ding, S., Wu, B. & Chen, W. Dominant characteristics of early autumn Arctic sea ice variability and its impact on Winter Eurasian climate. *J. Clim.* **34**, 1825–1846 (2021).
15. Baldwin, M. P. & Dunkerton, T. J. Stratospheric harbingers of anomalous weather regimes. *Science* **294**, 581–584 (2001).
16. Kolstad, E. W., Breiteig, T. & Scaife, A. A. The association between stratospheric weak polar vortex events and cold air outbreaks in the Northern Hemisphere. *Q. J. R. Meteorol. Soc.* **136**, 886–893 (2010).
17. Kretschmer, M. et al. More-persistent weak stratospheric polar vortex states linked to cold extremes. *Bull. Am. Meteorol. Soc.* **99**, 49–60 (2018).
18. Zuev, V. V. & Savelieva, E. Arctic polar vortex splitting in early January: the role of Arctic sea ice loss. *J. Atmos. Sol. Terr. Phys.* **195**, 105137 (2019).
19. Zhang, P., Wu, Y., Chen, G. & Yu, Y. North American cold events following sudden stratospheric warming in the presence of low Barents-Kara Sea sea ice. *Environ. Res. Lett.* **15**, 124017 (2020).
20. Barnes, E. A. & Screen, J. A. The impact of Arctic warming on the midlatitude jet-stream: can it? has it? will it? *Wiley Interdiscip. Rev. Clim. Change* **6**, 277–286 (2015).
21. Francis, J. A. Why are Arctic linkages to extreme weather still up in the air? *Bull. Am. Meteorol. Soc.* **98**, 2551–2557 (2017).
22. Cohen, J. et al. Divergent consensuses on Arctic amplification influence on midlatitude severe winter weather. *Nat. Clim. Change* **10**, 20–29 (2020).
23. Overland, J. E. et al. How do intermittency and simultaneous processes obfuscate the Arctic influence on midlatitude winter extreme weather events? *Environ. Res. Lett.* **16**, 043002 (2021).
24. Smith, D. M. et al. Robust but weak winter atmospheric circulation response to future Arctic sea ice loss. *Nat. Commun.* **13**, 1–15 (2022).
25. McCusker, K. E., Fyfe, J. C. & Sigmond, M. Twenty-five winters of unexpected Eurasian cooling unlikely due to Arctic sea-ice loss. *Nat. Geosci.* **9**, 838–842 (2016).
26. Seviour, W. J. Weakening and shift of the Arctic stratospheric polar vortex: Internal variability or forced response? *Geophys. Res. Lett.* **44**, 3365–3373 (2017).
27. Guan, W., Jiang, X., Ren, X., Chen, G. & Ding, Q. Role of atmospheric variability in driving the "warm-arctic, cold-continent" pattern over the North America sector and sea ice variability over the Chukchi-Bering sea. *Geophys. Res. Lett.* **47**, e2020GL088599 (2020).
28. Kretschmer, M., Zappa, G. & Shepherd, T. G. The role of Barents–Kara sea ice loss in projected polar vortex changes. *Weather Clim. Dyn.* **1**, 715–730 (2020).
29. Blackport, R. & Screen, J. A. Weakened evidence for mid-latitude impacts of Arctic warming. *Nat. Clim. Change* **10**, 1065–1066 (2020).
30. Blackport, R. & Screen, J. A. Observed statistical connections overestimate the causal effects of Arctic Sea ice changes on midlatitude winter climate. *J. Clim.* **34**, 3021–3038 (2021).
31. McKenna, C. M., Bracegirdle, T. J., Shuckburgh, E. F., Haynes, P. H. & Joshi, M. M. Arctic sea ice loss in different regions leads to contrasting Northern Hemisphere impacts. *Geophys. Res. Lett.* **45**, 945–954 (2018).
32. Jaiser, R., Dethloff, K. & Handorf, D. Stratospheric response to Arctic sea ice retreat and associated planetary wave propagation changes. *Tellus A Dyn. Meteorol. Oceanogr.* **65**, 19375 (2013).
33. Ruggieri, P., Kucharski, F., Buizza, R. & Ambaum, M. H. P. The transient atmospheric response to a reduction of sea-ice cover in the Barents and Kara Seas. *Q. J. R. Meteorol. Soc.* **143**, 1632–1640 (2017).
34. Blackport, R. & Screen, J. A. Influence of Arctic sea ice loss in autumn compared to that in winter on the atmospheric circulation. *Geophys. Res. Lett.* **46**, 2213–2221 (2019).
35. Baldwin, M. P. et al. The quasi-biennial oscillation. *Rev. Geophys.* **39**, 179–229 (2001).
36. Holton, J. R. & Tan, H. C. The influence of the equatorial quasi-biennial oscillation on the global circulation at 50 mb. *J. Atmos. Sci.* **37**, 2200–2208 (1980).
37. Butler, A. H. & Polvani, L. M. El Niño, La Niña, and stratospheric sudden warmings: a reevaluation in light of the observational record. *Geophys. Res. Lett.* **38** (2011).
38. Labe, Z., Peings, Y. & Magnusdottir, G. The effect of QBO phase on the atmospheric response to projected Arctic sea ice loss in early winter. *Geophys. Res. Lett.* **46**, 7663–7671 (2019).
39. Anstey, J. A. et al. Teleconnections of the quasi-biennial oscillation in a multi-model ensemble of QBO-resolving models. *Q. J. R. Meteorol. Soc.* **148**, 1568–1592 (2021).
40. Meredith, et al. In *IPCC Special Report on the Ocean and Cryosphere in a Changing Climate.* Ch. 3 (2019).
41. Simmonds, I. & Li, M. Trends and variability in polar sea ice, global atmospheric circulations, and baroclinicity. *Ann. N. Y. Acad. Sci.* **1504**, 167–186 (2021).
42. Matsuno, T. A dynamical model of the stratospheric sudden warming. *J. Atmos. Sci.* **28**, 1479–1494 (1971).
43. Polvani, L. M. & Waugh, D. W. Upward wave activity flux as a precursor to extreme stratospheric events and subsequent anomalous surface weather regimes. *J. Clim.* **17**, 3548–3554 (2004).
44. Nishii, K., Nakamura, H. & Miyasaka, T. Modulations in the planetary wave field induced by upward-propagating Rossby wave packets prior to stratospheric sudden warming events: a case-study. *Q. J. R. Meteorol. Soc.* **135**, 39–52 (2009).
45. Hoshi, K. et al. Poleward eddy heat flux anomalies associated with recent Arctic sea ice loss. *Geophys. Res. Lett.* **44**, 446–454 (2017).
46. Nishii, K., Nakamura, H. & Orsolini, Y. J. Geographical dependence observed in blocking high influence on the stratospheric variability through enhancement and suppression of upward planetary-wave propagation. *J. Clim.* **24**, 6408–6423 (2011).
47. Orsolini, Y. J., Nishii, K. & Nakamura, H. Duration and decay of Arctic stratospheric vortex events in the ECMWF seasonal forecast model. *Q. J. R. Meteorol. Soc.* **144**, 2876–2888 (2018).
48. Smith, K. L., & Kushner, P. J. Linear interference and the initiation of extratropical stratosphere-troposphere interactions. *J. Geophys. Res. Atmos.* **117** (2012).
49. Kobayashi, S. et al. The JRA-55 reanalysis: general specifications and basic characteristics. *J. Meteorol. Soc. Jpn. Ser. II* **93**, 5–48 (2015).
50. Mitchell, D. M. et al. The effect of climate change on the variability of the Northern Hemisphere stratospheric polar vortex. *J. Atmos. Sci.* **69**, 2608–2618 (2012).
51. Schimanke, S., Spangehl, T., Huebener, H. & Cubasch, U. Variability and trends of major stratospheric warmings in simulations under constant and increasing GHG concentrations. *Clim. Dyn.* **40**, 1733–1747 (2013).

52. Ayarzagüena, B. et al. No robust evidence of future changes in major stratospheric sudden warmings: a multi-model assessment from CCMI. *Atmos. Chem. Phys.* **18**, 11277–11287 (2018).

53. Cohen, J., Agel, L., Barlow, M., Garfinkel, C. I. & White, I. Linking Arctic variability and change with extreme winter weather in the United States. *Science* **373**, 1116–1121 (2021).

54. Yamazaki, K., Nakamura, T., Ukita, J. & Hoshi, K. A tropospheric pathway of the stratospheric quasi-biennial oscillation (QBO) impact on the boreal winter polar vortex. *Atmos. Chem. Phys.* **20**, 5111–5127 (2020).

55. Gettelman, A. et al. The whole atmosphere community climate model version 6 (WACCM6). *J. Geophys. Res. Atmos.* **124**, 12380–12403 (2019).

56. Fu, Q. et al. Quasi-biennial oscillation and sudden stratospheric warmings during the last glacial maximum. *Atmosphere* **11**, 943 (2020).

57. Charlton-Perez, A. J., Polvani, L. M., Austin, J., & Li, F. The frequency and dynamics of stratospheric sudden warmings in the 21st century. *J. Geophys. Res. Atmos.* **113** (2008).

58. McLandress, C. & Shepherd, T. G. Impact of climate change on stratospheric sudden warmings as simulated by the Canadian Middle Atmosphere Model. *J. Clim.* **22**, 5449–5463 (2009).

59. Hurrell, J. W., Hack, J. J., Shea, D., Caron, J. M. & Rosinski, J. A new sea surface temperature and sea ice boundary dataset for the Community Atmosphere Model. *J. Clim.* **21**, 5145–5153 (2008).

60. Kay, J. E. et al. The community earth system model (CESM) large ensemble project: a community resource for studying climate change in the presence of internal climate variability. *Bull. Am. Meteorol. Soc.* https://doi.org/10.1175/BAMS-D-13-00255.1 (2015).

61. Screen, J. A., Deser, C., Simmonds, I. & Tomas, R. Atmospheric impacts of Arctic sea-ice loss, 1979–2009: Separating forced change from atmospheric internal variability. *Clim. Dyn.* **43**, 333–344 (2014).

62. Charlton, A. J. & Polvani, L. M. A new look at stratospheric sudden warmings. Part I: climatology and modeling benchmarks. *J. Clim.* **20**, 449–469 (2007).

63. Charlton, A. J. et al. A new look at stratospheric sudden warmings. Part II: evaluation of numerical model simulations. *J. Clim.* **20**, 470–488 (2007).

64. Choi, H., Kim, B. M. & Choi, W. Type classification of sudden stratospheric warming based on pre-and postwarming periods. *J. Clim.* **32**, 2349–2367 (2019).

65. Andrews, D. G., Holton, J. R., & Leovy, C. B. *Middle Atmosphere Dynamics* Vol. 40. (Academic Press, 1987).

66. Plumb, R. A. On the three-dimensional propagation of stationary waves. *J. Atmos. Sci.* **42**, 217–229 (1985).

67. Vallis, G. K. *Atmospheric and Oceanic Fluid Dynamics* (Cambridge Univ. Press, 2017).

68. Newman, P. A., Coy, L., Pawson, S. & Lait, L. R. The anomalous change in the QBO in 2015–2016. *Geophys. Res. Lett.* **43**, 8791–8797 (2016).

AUTHOR CONTRIBUTIONS

J.Z. performed the WACCM6 simulations and the analyses in discussion with Y.J.O. and V.L. All authors interpreted and discussed the results. J.Z. drafted the manuscript with the other authors contributing to its content. All authors approved the final manuscript.

COMPETING INTERESTS

The authors declare no competing interests.

ADDITIONAL INFORMATION

Supplementary information The online version contains supplementary material available at https://doi.org/10.1038/s41612-022-00296-w.

Correspondence and requests for materials should be addressed to Jiarong Zhang.

Reprints and permission information is available at http://www.nature.com/reprints

Publisher's note Springer Nature remains neutral with regard to jurisdictional claims in published maps and institutional affiliations.